Pattern formation arising from condensation of a homogeneous gas into a binary, phase-separating liquid

C. M. Pooley and Anna C. Balazs
Chemical and Petroleum Engineering Department, University of Pittsburgh, Pittsburgh, Pennsylvania 15261, USA

J. M. Yeomans
The Rudolf Peierls Centre for Theoretical Physics, Oxford University, 1 Keble Road, Oxford OX1 3NP, United Kingdom
(Received 12 April 2005; published 16 August 2005)

We examine the nucleated growth of a binary, immiscible liquid drop within a homogeneous gas. The system couples the growth of the liquid drop with the phase separation of the immiscible components and, thus, can potentially reveal novel pattern formation. To carry out this study, we first characterize the thermodynamic properties of the system in terms of an appropriate Ginzburg-Landau free energy density. By minimizing this free energy, we construct the equilibrium phase diagram for the system. We then use a lattice Boltzmann algorithm to solve the hydrodynamic equations describing the dynamical evolution of the fluid. We observe intriguing tentaclelike structures within the nucleation and growth regime and explore how the formation of these structures depends on the thermodynamic and transport properties of the system. We give scaling laws describing domain growth in both the diffusion- and flow-limited regimes. The results highlight the novel physics that can emerge when there is interplay between the ordering of a density and a concentration field.

DOI: 10.1103/PhysRevE.72.021505 PACS number(s): 64.75.+g, 47.54.+r, 47.20.−k, 05.70.Ce

I. INTRODUCTION

Pattern formation through phase separation is a topic of continuous interest to both theorists and experimentalists [1]. For example, the complex morphologies formed by binary, immiscible mixtures are still a topic of extensive study [2,3]. There remains, however, an intriguing phase-separating system that has not been extensively investigated; namely, a homogeneous gas that condenses into an AB binary liquid. Here, the phase separation between the two components, A and B, occurs inside the growing liquid domains. Consequently, there are two distinct length scales that characterize the system: the average size of liquid domains and the size of the A/B regions. Synergistic interactions between the growth of the liquid phase and the A/B phase separation can lead to novel behavior, which is both intrinsically interesting and of practical importance for optimizing various separation processes [4].

The existing theoretical studies on this system involved thermodynamic calculations and led to some ambiguity concerning the morphology of the nucleated fluid [5–7]. Near the liquid/gas critical point, however, thermodynamics and hydrodynamics are highly coupled [8] and approaches that incorporate this coupling could elucidate the structural evolution of the multiphase mixture. Here, we use information about the thermodynamic state of the system to undertake the first hydrodynamic studies of the nucleated growth of a binary, immiscible fluid drop within a homogeneous gas. Using this approach, we characterize the structure formation and the rate of domain growth in the system. In particular, we observe that the liquid phase forms striated "tentaclelike" structures, which grow linearly with time.

In Sec. II, we describe a mean field model of this system. In Sec. III we give a brief summary of the lattice Boltzmann method, a standard technique for numerically modeling the continuum equations. In Sec. IV, we give the simulation results, and in Sec. V, we discuss these results and propose simple scaling arguments, which give the growth rates for the nucleated droplet in the diffusion- and flow-limited cases. In the conclusions, we map our simulation results onto real, physical parameters in order to facilitate experimental studies on this system.

II. THE MODEL

The system is modeled by considering two species of particles, A and B. The particles have hard cores and experience a mutual long range attractive interaction, which gives rise to the liquid-gas phase transition. However, the interactions between like and unlike particles are not equal, resulting in the binary phase separation within the liquid phase.

The Ginzburg-Landau free energy functional for the system is given by

$$\Psi = \int \left(\psi + \frac{\kappa_\varphi}{2} |\nabla \varphi|^2 + \frac{\kappa_\rho}{2} |\nabla \rho|^2 \right) d\mathbf{r}. \tag{1}$$

The gradient squared terms describe the surface tensions between the liquid-gas and liquid-liquid phases. The bulk free energy density is given by

$$\psi = \theta \left[\frac{\rho+\varphi}{2} \ln\left(\frac{\rho+\varphi}{2}\right) + \frac{\rho-\varphi}{2} \ln\left(\frac{\rho-\varphi}{2}\right) - \rho \ln(1-b\rho) \right] - a\rho^2 + \lambda(\rho^2 - \varphi^2), \tag{2}$$

where $\rho=\rho_A+\rho_B$ is the total mass density, $\varphi=\rho_A-\rho_B$ is the mass density difference between species, and $\theta=k_BT/m$ is a reduced temperature. The parameters b, a, and λ account for the excluded volume of particles, a mutual attraction, and a repulsive interspecies interaction, respectively. A detailed de-

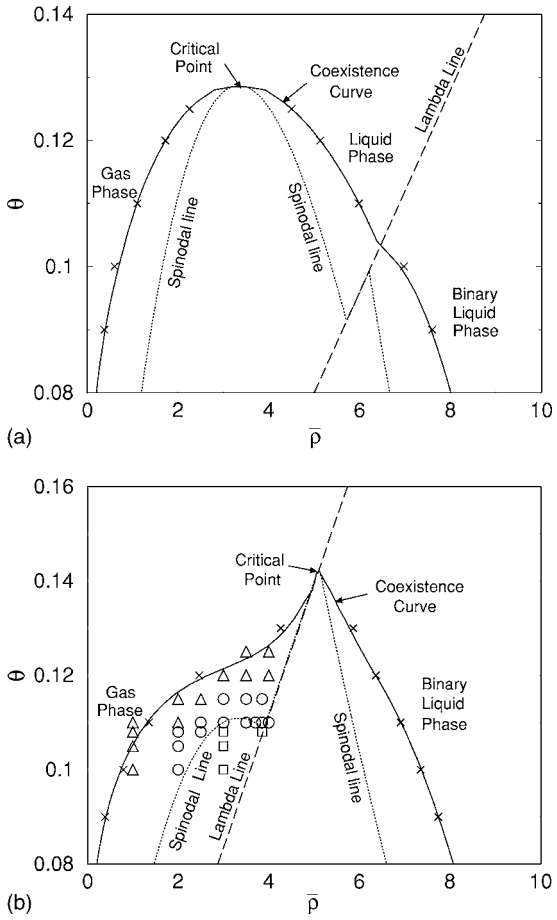

FIG. 1. The phase diagrams for two different values of the interspecies interaction strength λ. They show the behavior of a system with an average density $\bar{\rho}$ and temperature θ. If the temperature is below the critical point, and $\bar{\rho}$ lies between the two solid curves, then the system lowers its free energy by phase separating into a liquid and a gas phase. The lambda line divides binary states to the right from homogeneous states to the left. The spinodal line encloses states that spontaneously phase separate. (a) A weaker interspecies interaction, $\lambda=0.008$. (b) A stronger interspecies interaction, $\lambda=0.014$. The following symbols mark these specific cases: ×, simulation results of the coexistence curve; ○, nucleated tentacle structures; △, no tentacles form; and □, spinodal decomposition.

scription of how ψ is derived is given in the Appendix. From Eq. (2), we can obtain the pressure, which is given by [9]

$$p_0 = \rho\frac{\partial\psi}{\partial\rho} + \varphi\frac{\partial\psi}{\partial\varphi} - \psi = \frac{\rho\theta}{1-\rho b} - a\rho^2 + \lambda(\rho^2 - \varphi^2). \quad (3)$$

Note that if we set $\lambda=0$, then equation (3) reduces to the normal van der Waals equation of state.

Figure 1 shows phase diagrams obtained for two different interaction strengths, $\lambda=0.008$ and $\lambda=0.014$. They indicate the behavior of a system with an average density $\bar{\rho}$ and temperature θ. The area between the spinodal lines defines the spinodal region. For a uniform system that is quenched into this region, any arbitrarily small perturbation will grow, and spinodal decomposition will result. We note that the average density $\bar{\rho}$ can lie within the nucleation and growth region, which lies outside the spinodal region, but within the coexistence curve. In this case, even if the system is perturbed, it cannot phase separate, even though it is energetically favorable to do so. It is necessary to have some kind of nucleation. This nucleating agent can either be a region of phase-separated fluid, or some kind of particle, whose surface is preferentially wetting. Once initiated, the nucleated region can grow and allow the rest of the system to reach its energetic ground state.

The dynamic behavior of the above system is described by the following equations [9]:

$$\partial_t\rho + \partial_\alpha(\rho u_\alpha) = 0,$$

$$\partial_t(\rho u_\alpha) + \partial_\beta(\rho u_\alpha u_\beta) = -\partial_\beta P_{\alpha\beta} + \partial_\beta\sigma_{\alpha\beta},$$

$$\partial_t\varphi + \partial_\alpha(\varphi u_\alpha) = M\nabla^2\mu_\varphi. \quad (4)$$

Here, u_α is the fluid velocity, $\sigma_{\alpha\beta}$ is the viscous stress tensor, and M is the mobility. The chemical potential and pressure tensor in Eq. (4) depend on the thermodynamic properties of the system. In particular, the chemical potential is defined by

$$\mu_\varphi = \frac{\delta\Psi}{\delta\varphi} = \frac{\theta}{2}\ln\left(\frac{\rho+\varphi}{\rho-\varphi}\right) - 2\lambda\varphi - \kappa_\varphi\nabla^2\varphi. \quad (5)$$

The pressure tensor, in turn, is given by [11]

$$P_{\alpha\beta} = p\,\delta_{\alpha\beta} + \kappa_\varphi\partial_\alpha\varphi\,\partial_\beta\varphi + \kappa_\rho\partial_\alpha\rho\,\partial_\beta\rho, \quad (6)$$

where

$$p = p_0 - \kappa_\varphi\varphi\nabla^2\varphi - \frac{\kappa_\varphi}{2}|\nabla\varphi|^2 - \kappa_\rho\rho\nabla^2\rho - \frac{\kappa_\rho}{2}|\nabla\rho|^2. \quad (7)$$

These equations ensure the conservation of the total mass of each component, and the total momentum, and are free energy minimizing. The equations are solved numerically using a lattice Boltzmann algorithm, which is detailed below.

III. THE LATTICE BOLTZMANN METHOD

The lattice Boltzmann (LB) algorithm is now a widely used method for studying the dynamic behavior of multiphase flows. The classic LB model consists of a set of particle distribution functions moving on a regular grid. The distribution functions are moved from site to site at each time step, and undergo collisions at each site. The collisions allow the distribution functions to reach local equilibrium and are chosen to conserve mass and momentum. It can be shown that the model reduces to the standard Navier-Stokes equation in the continuum limit [10]. The LB model, however, solves the equation indirectly, rather than directly, as in conventional computational fluid dynamics (CFD).

Our model is essentially a combination of the liquid-gas and binary fluid lattice Boltzmann models proposed by Swift *et al.* [11]. The equations are solved on a square lattice in two dimensions (2D) and on a cubic lattice in 3D. The distribution functions f_i and g_i give the density and density difference, respectively, of the particle populations that make up the system. Here, the subscript i refers to the velocity

direction. In 2D, there are nine velocities $\mathbf{e}_i$, which move particles between nearest and next-nearest neighbors in a time Δt. We use a 15-velocity model in 3D. The evolution in time of the distribution functions is given by

$$f_i(\mathbf{r}+\mathbf{e}_i\Delta t, t+\Delta t) = f_i(\mathbf{r},t) - \frac{1}{\tau_\rho}[f_i(\mathbf{r}) - f_i^{eq}(\mathbf{r})],$$

$$g_i(\mathbf{r}+\mathbf{e}_i\Delta t, t+\Delta t) = g_i(\mathbf{r},t) - \frac{1}{\tau_\varphi}[g_i(\mathbf{r}) - g_i^{eq}(\mathbf{r})]. \quad (8)$$

The parameters τ_ρ and τ_φ characterize how the system relaxes toward equilibrium, and are related to the viscosity of the fluid and the mobility of particles, respectively. The physical variables are calculated from the distribution functions by

$$\rho = \sum_i f_i, \quad \varphi = \sum_i g_i, \quad \rho u_\alpha = \sum_i f_i e_{i\alpha}. \quad (9)$$

For mass and momentum conservation,

$$\sum_i f_i^{eq} = \rho, \quad \sum_i g_i^{eq} = \varphi, \quad \sum_i f_i^{eq} e_{i\alpha} = \rho u_\alpha. \quad (10)$$

The higher moments of the equilibrium distribution are chosen to give the correct continuum equations. An appropriate choice is

$$\sum_i g_i^{eq} e_{i\alpha} e_{i\beta} = \frac{M\mu_\varphi}{\Delta t\left(\tau_\varphi - \frac{1}{2}\right)}\delta_{\alpha\beta} + \varphi u_\alpha u_\beta, \quad (11)$$

$$\sum_i f_i^{eq} e_{i\alpha} e_{i\beta} = P_{\alpha\beta} + \rho u_\alpha u_\beta + \nu\left(1 - \frac{3}{c^2}\frac{dp_0}{d\rho}\right) \times (u_\alpha \partial_\beta \rho + u_\beta \partial_\alpha \rho + \delta_{\alpha\beta} u_\gamma \partial_\gamma \rho), \quad (12)$$

$$\sum_i f_i^{eq} e_{i\alpha} e_{i\beta} e_{i\gamma} = \frac{\rho c^2}{3}(\delta_{\alpha\beta} u_\gamma + \delta_{\alpha\gamma} u_\beta + \delta_{\beta\gamma} u_\alpha), \quad (13)$$

where ν is the kinematic viscosity. The parameter Δx is the grid spacing, and $c = \Delta x/\Delta t$ is the lattice velocity. Note that the last term in Eq. (12) is necessary for ensuring Galilean invariance [10].

By performing a Chapman-Enskog expansion [12], which corresponds to an expansion of equations (8) in a power series in Δt and Δx, it is possible to recover the continuum equations, with a viscous stress tensor given by

$$\sigma_{\alpha\beta} = \rho\nu\left(\partial_\alpha u_\beta + \partial_\beta u_\alpha + \left(1 - \frac{3}{c^2}\frac{dp_0}{d\rho}\right)\delta_{\alpha\beta}\partial_\gamma u_\gamma\right), \quad (14)$$

where the kinematic viscosity is

$$\nu = \frac{\Delta x^2\left(\tau_\rho - \frac{1}{2}\right)}{3\,\Delta t}. \quad (15)$$

IV. NUMERICAL SIMULATIONS

The simulations were performed on a two-dimensional (2-D) grid of size $L_x = 1024$ and $L_y = 1024$, with periodic boundary conditions imposed in both directions. The values of $\kappa_\rho = 0.015$ and $\kappa_\varphi = 0.015$ were chosen to give interface widths of approximately four lattice sites. Other parameters were $\tau_\varphi = 1$, and $\Delta x = 1$. Viscosity was changed by varying the time step within the range $\Delta t = 0.1 - 0.4$, and the relaxation parameter within the range $\tau_\rho = 0.55 - 2$ [13].

To test our LB algorithm, we performed 1-D simulations to numerically calculate the liquid and gas coexisting densities. Our results are indicated by the crosses on the phase diagrams in Fig. 1; as can be seen, we obtain good agreement with the theoretical thermodynamic calculations. The small deviations were caused by the finite interface width.

In this paper, we focus on nucleated growth. An initially circular region of liquid A, with radius $r = 13$, was placed at the center of an otherwise uniform system of density $\bar{\rho} = 3.85$ and density difference $\bar{\varphi} = 0$. A small random noise was added to ρ and φ to break the symmetry. The parameters used were mobility $M = 10$, temperature $\theta = 0.11$, interaction strength $\lambda = 0.014$, and kinematic viscosity $\nu = 1$. Note that on the phase diagram 1(b), this initial state lies just outside of the spinodal region, within the nucleation and growth regime. Figure 2(a) reveals the evolution of the density difference φ as a function of time for this system. Rather than simply growing in a roughly circular manner (as happens in the case of a single component liquid-gas system), we discover the formation of outwardly radiating, striped tentacles.

To understand this behavior, we note that, initially, the pressure in the nucleating droplet is lower than that of the surrounding gas. In order for the droplet to equilibrate with these surroundings, it consumes some of the nearby gas and thereby swells. As this fluid is deposited, it phase separates. The resulting "bullseye" pattern, which has alternating concentric circles of A-rich and B-rich fluid, has been previously observed in nucleated binary liquids [14]. However, in that case, the structure was found to be a short lived, transient state. In our case, we observe that the deposition of the phase-separated liquid is not uniform. Rather than forming a thin coating, it forms droplets on the surface, as illustrated in the second frame of Fig. 2(a). One possible reason for the coating of droplets (rather than a uniform film) is that this structure corresponds to a lower energetic state, because it results in the creation of less interfacial area for a given volume of deposited liquid. After the surface droplets form, the pressure in the gas just outside their tips is found to be less than that in the surrounding area. This preferentially drives fluid toward these regions and results in clearly defined branches that grow outward. The reason for this variation in pressure is due to surface tension. The pressure difference between the interior and exterior of an interface, with radius of curvature R, is given by $\Delta p = p^{int} - p^{ext} = \sigma/R$. Since the radius of curvature is smallest at the tips of the drop, the pressure in the gas phase surrounding these regions, p^{ext}, is lowest.

We measure the growth of these structures in the following way. We calculate the geometric center of the liquid region, and then consider concentric circles of a given radius that are drawn around this central point. If the circle just touches the outermost tip of the farthest tentacle, then this is defined to be the tip radius. If the circle passes through an equal amount of liquid and gas, then this is called the core

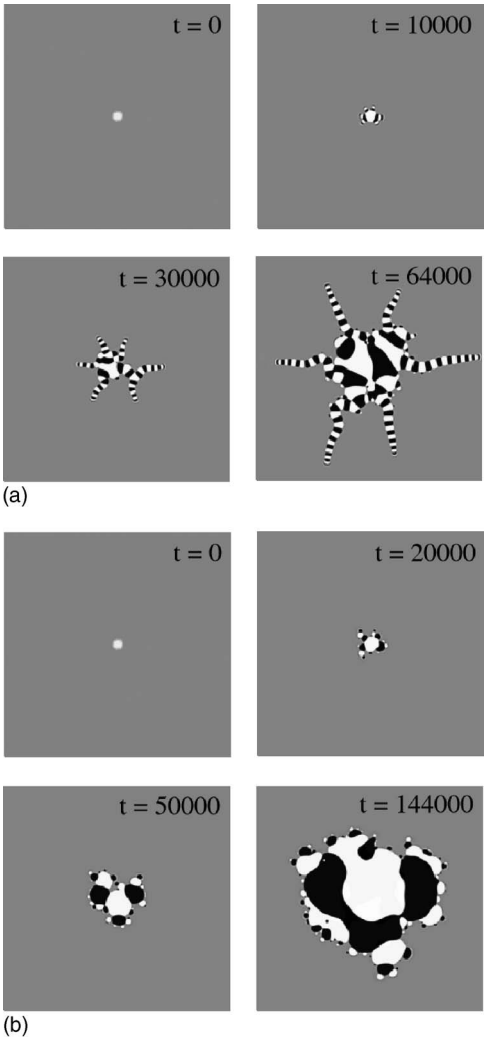

FIG. 2. The time evolution of the density difference profile φ across the system. The time is measured in lattice units. Black and white areas denote the A-rich and B-rich liquid, respectively, and gray areas represent gas. (a) High viscosity $\nu=1$. (b) Low viscosity $\nu=0.125$.

radius. Figure 3(a) shows how the tip radius (solid line) and core radius (dashed line) change in time, for a system with viscosity $\upsilon=1$ and mobility $M=10$. We find that there is a linear relationship in both cases.

The rate of growth of the radii was found by performing a linear regression on these curves and calculating the slope. By changing the viscosity of the fluid, we discover that these growth rates vary, as illustrated in Fig. 3(b). At low viscosities, the tentacles no longer appear, as indicated by the fact that the growth rate of the tip is almost equal to that of the core. An example of this regime is shown in Fig. 2(b). Here, the viscosity was $\nu=0.125$, and the mobility was $M=10$. We observe mixing within the core region, which becomes increasingly active as the viscosity is decreased. This mixing is due to extensive flow, which makes the tentacle formation unstable. It was not possible to probe very low viscosities, as the simulations become numerically unstable.

Figure 3(c) shows the growth rate of the radii as a function of mobility M, for a viscosity of $\nu=0.5$. We find that

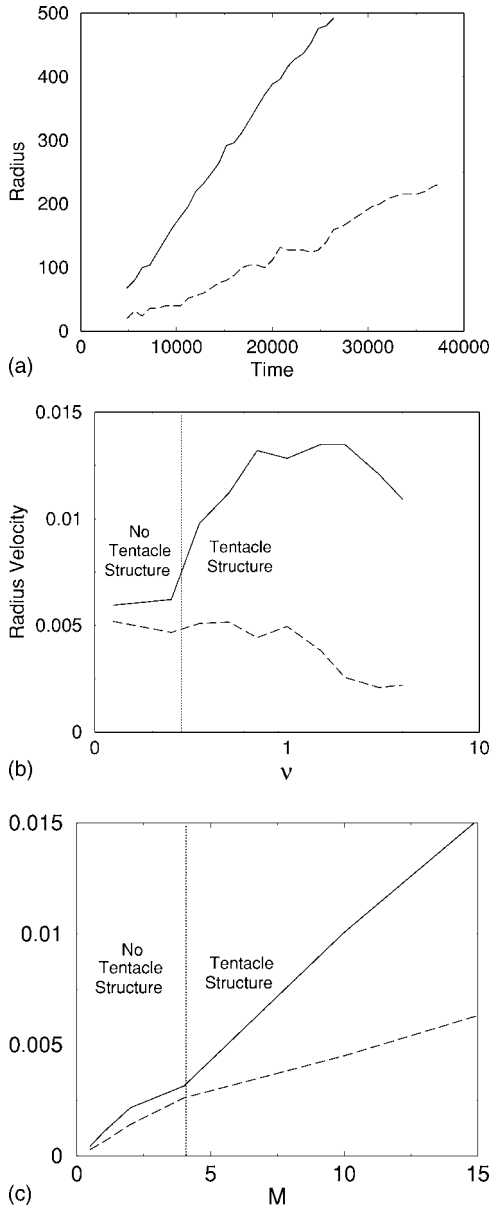

FIG. 3. (a) The variation in time of the tip radius (solid lines) and the core radius (dashed lines). The viscosity was $\nu=1$ and the mobility was $M=10$. The time is measured in lattice units. By taking a linear regression, the tip and core radius growth rates were found to be 0.020 and 0.0068, respectively. (b) The variation of tip and core radius growth rates as a function of kinematic viscosity ν, with fixed mobility $M=10$. The dotted line shows the transition between the droplet forming/not forming a tentacle structure. (c) The variation of tip and core radius growth rates as a function of mobility M. The viscosity was $\nu=0.5$.

these rates are approximately proportional to the mobility M, suggesting that the nucleated droplet growth is limited by interparticle diffusion (see Sec. V A). Note, also, that there exists a transition from no tentacles to tentacles at around $M=4$. From this, and the results in Fig. 3(b), we conclude that this transition occurs between low viscosity, low mobility and high viscosity, high mobility.

On the phase diagram 1(b), the triangles △, squares □, and circles ○ show where simulations have been performed,

(a)

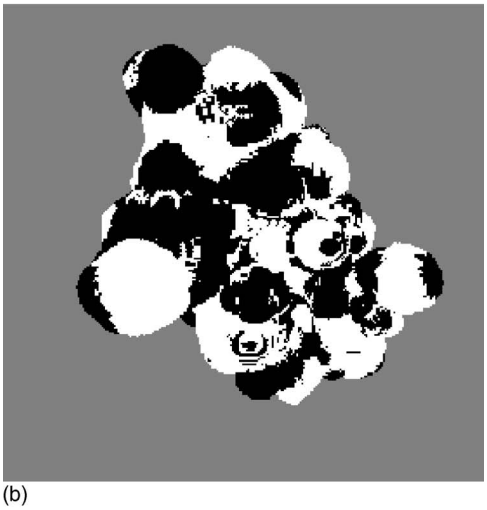

(b)

FIG. 4. Snapshots, shown in perspective, of nucleated droplets in 3D (the gas phase is transparent). Black and white areas are the A-rich and B-rich liquid, respectively. The mobility was $M=5$. (a) Snapshot at $t=9000$ with high viscosity $\nu=2$. (b) Snapshot at $t=7800$ with low viscosity $\nu=0.1$.

to help delineate the region in phase space where the tentacle structures form. We find that the structures are more articulated (i.e., have a larger ratio of tip to core radius) as the compositions get closer to the spinodal curve (see 1(b)). The results of all our simulations revealed structures with either four, five, or six tentacles, depending upon the random initial conditions.

By changing the variable κ_φ, it was possible to vary w, the width of the interface between the A/B domains. Through this variation, we found that the width of the stripes within the tentacles is proportional to w.

Simulations were also performed in 3D in order to determine if the 3-D behavior is qualitatively similar to the 2-D case. The size of the system was taken to be $L_x=190$, $L_y=190$, and $L_z=190$. The following values of the parameters were used in the 3-D simulations: $\kappa_\rho=\kappa_\varphi=0.0075$, $\bar{\rho}=3.85$, $\theta=0.11$, and $M=5$. An initially spherical, nucleating A-rich liquid region, of radius $r=3$, was placed at the center of the

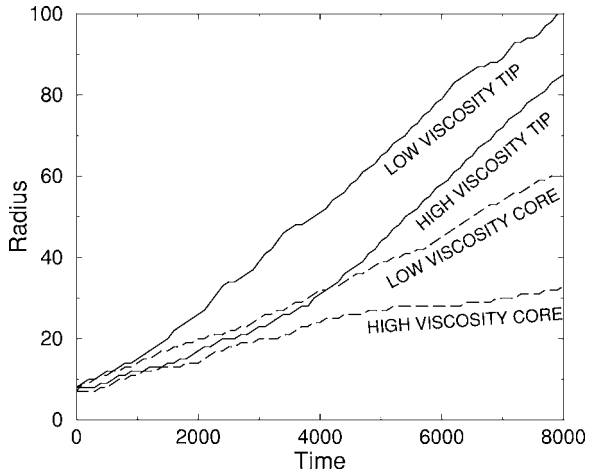

FIG. 5. The core and tip radii of a 3-D droplet, as a function of time. The low viscosity was $\nu=0.1$ and the high viscosity was $\nu=2$. The mobility was $M=5$.

system. Figure 4 shows snapshots (shown in a perspective view) of the 3-D droplets that are formed after some time. In Fig. 4(a), we observe that the fluid was deposited onto the droplet in alternating A-rich and B-rich layers, and that tentacles formed in much the same way as in Fig. 2(a). The 3-D simulations are computationally intensive, requiring long run times. Consequently, the final state shown in Fig. 4(a) still represents a relatively early stage in the droplet development, as compared to the 2-D case. However, we expect that in time, the tentacles would extend and become increasingly well defined. Figure 4(b) shows that at low viscosities, tentacles do not form. Analogous to Fig. 2(b), extensive mixing is observed within the core. Figure 5 shows how the droplet radius grows as a function of time, at both high and low viscosities for these 3-D studies. Both plots are found to be linear in the long time limit. The ratio of the tip to core growth rate at the end of the simulation is found to be much larger in the high viscosity case, indicative of the tentacle growth.

V. DISCUSSION AND SCALING ANALYSIS

The long time linear growth of the droplets can be explained using simple scaling arguments. Figure 6 shows a contour plot of the free energy density ψ (see Eq. (2)), below the critical temperature (in this case $\theta=0.11$), as a function of density ρ and density difference φ. The dark regions mark areas of the lowest free energy, while the light regions mark the highest free energy. The three black areas show the coexisting equilibrium states: homogeneous gas, A-rich liquid, and B-rich liquid. In transforming from the initially quenched density $\bar{\rho}$ to the phase separated state, part of the fluid follows path 1 and becomes gas, and part becomes liquid, by following the two curves marked by 2 on this diagram. Note, that these paths follow the lines of steepest descent. The fluid does not follow the dashed path, marked by 3, i.e., it does not first undergo liquid-gas phase separation and then liquid-liquid (A/B) phase separation. The latter route is not energetically favorable, because the intermediate

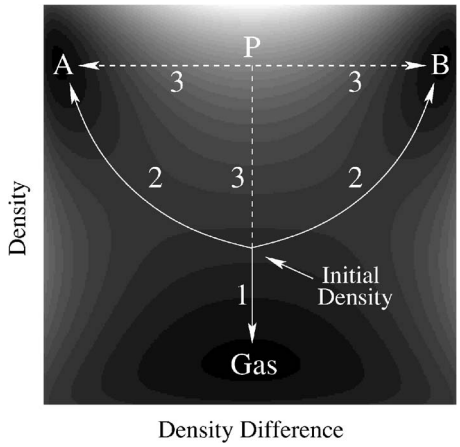

FIG. 6. A contour plot of the free energy density ψ (see Eq. (2)) [15]. The three minima show the coexistence between the gas and liquid A-rich and B-rich phases.

point P has a substantially higher energy density. Therefore, both particle diffusion and gas flow into the liquid are simultaneously involved in the growth of the droplet. Hence two limiting cases exist; these are described below.

A. Growth limited by diffusion

We first consider the case where the mobility of the particles (and/or the viscosity) is sufficiently low that the interparticle diffusion is the limiting factor in the growth of the droplet. That is, as the droplet grows, gas is deposited onto the surface and phase separates into A-rich and B-rich layers, which are sequentially added onto the outside of the droplet. We now approximately calculate the time it takes for this homogeneous fluid to phase separate into alternating A/B stripes, of width $\sim 2w$. By substituting wave solutions of the form $\varphi = Ae^{\Gamma t}\sin(\pi x/w)$ into the Cahn-Hilliard equation, it is possible to obtain

$$\Gamma = \left(\frac{\pi}{w}\right)^2 M\left(\frac{2\lambda\rho_l - \theta}{\rho_l} - \kappa_\varphi\left(\frac{\pi}{w}\right)^2\right). \tag{16}$$

The inverse of this quantity gives the characteristic time for each stripe to form; hence, the growth rate of the radius can be approximated by

$$\frac{dr_d}{dt} \sim \pi^2 \frac{M}{w}\left(\frac{2\lambda\rho_l - \theta}{\rho_l} - \kappa_\varphi\left(\frac{\pi}{w}\right)^2\right), \tag{17}$$

where r_d is the radius of the droplet. The right-hand side of this equation is constant; therefore the growth of the droplet size is linear in time. Note that this equation also predicts that the growth rate is proportional to mobility M, in good agreement with Fig. 3(c).

B. Growth limited by viscous dissipation from flow

We expect that when the mobility is sufficiently high, or when the fluid is sufficiently viscous, growth would be limited by how fast the gas can flow and deposit onto the droplet surface. In this case, the binary nature of the fluid can be neglected. A simple understanding of this process can be gained through energetic considerations. We first describe the 2-D case. The change in the total bulk free energy of the system resulting from a variation in the radius r_d of the drop is given by

$$\frac{dF}{dr_d} = 2\pi\,\Delta\psi\, r_d, \tag{18}$$

where $\Delta\psi = \psi_{\bar\rho} - \psi_l - \mu_\rho(\bar\rho - \rho_l)$ is the excess free energy density difference between the initial density $\bar\rho$ and the final liquid density ρ_l. It is this energy that drives the droplet growth. We assume that the surrounding gaseous fluid is being radially deposited onto the surface, with a velocity u_s. Hence, the droplet growth is described by $dr_d/dt = (\bar\rho/\rho_l)u_s$ (assuming $\bar\rho \ll \rho_l$). Assuming approximate incompressibility for the gas, the velocity field, at position $\mathbf{r}$, has the form $\mathbf{u} = -(u_s r_d/r)\hat{\mathbf{r}}$ outside the drop, and $\mathbf{u} = \mathbf{0}$ inside the drop. The viscous dissipation can be estimated by considering the total dissipation of kinetic energy due to the stress tensor (given in Eq. (14)),

$$\int \sigma_{\alpha\beta}\partial_\beta u_\alpha d\mathbf{r} \simeq \bar\rho\nu u_s^2. \tag{19}$$

By equating energy liberation, Eq. (18), with viscous dissipation, Eq. (19), and energy taken up in creating additional interface, we find

$$2\pi\,\Delta\psi\, r_d \frac{\bar\rho}{\rho_l} u_s = \bar\rho\nu u_s^2 + 2\pi\sigma\frac{\bar\rho}{\rho_l}u_s, \tag{20}$$

where σ is the liquid-gas surface tension. We can rearrange this expression to find the velocity, and hence the growth rate

$$\frac{dr_d}{dt} = \frac{2\pi}{\bar\rho\nu}\left(\frac{\bar\rho}{\rho_l}\right)^2(\Delta\psi\, r_d - \sigma). \tag{21}$$

This equation shows the well-known result, that below a critical radius $r_d^{crit} = \sigma/\Delta\psi$, a droplet will evaporate because of the surface tension pushing inward. For a large radius r_d, this equation has the exponential solution

$$r_d = Ae^{(2\pi/\bar\rho\nu)(\bar\rho/\rho_l)^2\Delta\psi\, t}. \tag{22}$$

In Secs. V A and V B we gave a description of how the nucleated region grows. At very early times, the growth rate is small, and diffusion effects can be neglected. Equation (22) shows that in this regime the growth rate increases exponentially in time. When the growth rate becomes comparable to that in Eq. (17), then diffusion can no longer be ignored. Therefore, at late times we expect the drop growth to be limited to linear in time. By equating expressions (17) and (21), we obtain a typical radius that lies within the transition between these two regimes,

$$r_d^{tran} \simeq \frac{\pi\nu M\rho_l\left[2\lambda\rho_l - \theta - \left(\frac{\pi}{w}\right)^2\kappa_\varphi\rho_l\right]}{2w\,\Delta\psi\,\bar\rho}. \tag{23}$$

If typical simulation parameters are substituted into this expression $(\rho_l/\bar\rho \sim 6, M \sim 5, \nu \sim 1, \Delta\psi \sim 0.05, w \sim 4, 2\lambda\rho_l - \theta$

$\sim 0.1, \kappa \sim 0.01$), then we obtain $r_d^{tran} \sim 15$. Since this lies very early within our simulations (see Fig. 3(a)), it is difficult to observe the early time exponential behavior. However, the late time linear behavior (which occurs after this transition point) is clearly seen.

In 3D, an analysis gives the same growth rate, Eq. (22), and transitional radius, Eq. (23), up to a constant factor.

It must be noted that the arguments presented here describe only the average growth rates, and do not explain the observation of the tentacle structures.

VI. CONCLUSION

To summarize, we find that the mechanism for nucleated growth is quite different from that observed in single component fluids. The phase separation proceeds by long arms, extending from the nucleation region into the gas. Initially, growth is limited by flow, and has an exponential solution, but at a later time, diffusion limits the growth to being linear in time.

It would be of interest to see whether these structures could be observed experimentally. In mapping our simulation results onto a real system, we first discuss the relative importance of momentum and interparticle diffusion. This is characterized by the Schmidt number $\mathrm{Sc} = \nu/D$, where D is the diffusion constant, which is related to the mobility through $D = M[(2\lambda\rho_l - \theta)/\rho_l]$. For a typical gas $\mathrm{Sc} \sim 1$, and for a liquid $\mathrm{Sc} \sim 50$. The reason the Schmidt number is higher in the liquid case is that the fluid is sufficiently dense that particles become "caged in" by their neighbors; this inhibits particle mixing, but enhances momentum transfer because more collisions occur. In our simulations, the Schmidt number is in the range $\mathrm{Sc} \sim 1-40$, hence physically reasonable.

A typical fluid has density $\rho_r \simeq 10^3$ kg m^{-3}, kinematic viscosity $\nu_r \simeq 10^{-6}$ m^2 s^{-1}, and surface tension $\sigma_r \simeq 0.04$ N m^{-1}, where the subscript r denotes SI units. These parameters are related to the simulation variables through $\nu_r = \nu(\Delta t/\Delta x^2) \times (\Delta x_r^2/\Delta t_r)$, and $\sigma_r = \sigma(\Delta t^2/\rho\,\Delta x)(\rho_r \Delta x_r/\Delta t_r^2)$. In the simulations, $\rho \simeq 7$, $\nu \simeq 1$, and $\sigma \simeq 0.5$, in lattice units. Matching these respective quantities, we calculate the grid spacing to be around $\Delta x_r \simeq 2$ nm and time step $\Delta t_r \simeq 10^{-11}$ s. Since the interfaces are a few lattice sites wide, then the interface width is around 10 nm, in good agreement with that observed experimentally [16]. The snapshots in Fig. 2 correspond to the structure after ~ 1 μs, with a droplet diameter of around ~ 1 μm. It might not be feasible to experimentally observe such rapid growth in real time, however, the final state of the system could be frozen and then structurally analyzed. These values can serve as a guideline for directing experimental efforts along fruitful pathways. Note that within the simulations, we have neglected the effect of Brownian noise. It is possible that this may affect the stability of these structures at such small length scales. This will be the subject of future research.

Finally, we note that extensive work has been done on the domain growth of liquid-gas systems [17] and of binary systems [2], however, the system described herein remains relatively unexplored. The cooperative behavior between the phase-separating liquids and the growth of the liquid droplet can potentially reveal a wealth of interesting new physics and therefore warrants further investigation.

ACKNOWLEDGMENTS

The authors thank Dr. Enzo Orlandini for his useful help, and gratefully acknowledge the financial support from NSF and ONR.

APPENDIX: DERIVATION OF FREE ENERGY DENSITY

In this appendix, we derive the bulk free energy (2) by constructing a simple, 1-D statistical mechanical model. The length of the system is taken to be L. The partition function is given by

$$Z = \frac{1}{N_A!\,N_B!} \prod_{i,j} \int dp_i^{A,B} dx_i^{A,B} e^{-(1/k_B T)(p_i^{A,B^2}/2m_i^{A,B} + \Phi)}, \tag{A1}$$

where p_i and x_i denote the momentum and position of particles, T is the temperature, k_B is the Boltzmann constant, and N_A and N_B are the number of A and B particles, respectively. We make the mean field approximation by assuming that each particle feels an effective potential $\phi(x)$, which describes its interaction with all the other particles. This simplification allows us to separate the total potential energy, Φ, as follows:

$$\Phi = \left[\sum_{i=1}^{N_A} \phi_{AA}(x_i^A) + \phi_{AB}(x_i^A) \right] + \left[\sum_{i=1}^{N_B} \phi_{BA}(x_i^B) + \phi_{BB}(x_i^B) \right], \tag{A2}$$

where ϕ_{AB} is the potential of an A particle sitting in a field created by B, and a similar interpretation applies to the other ϕ terms. The partition function can then be written as

$$Z = \frac{1}{N_A!\,N_B!} \left[\int dp^A dx^A e^{-(1/k_B T)(p^{A^2}/2m^A + \phi_{AA} + \phi_{AB})} \right]^{N_A} \times \left[\int dp^B dx^B e^{-(1/k_B T)(p^{B^2}/2m^B + \phi_{BA} + \phi_{BB})} \right]^{N_B}. \tag{A3}$$

The momentum integrals are easily done:

$$\int dp^{A,B} e^{-p^{A,B^2}/2m^{A,B} k_B T} = \sqrt{2\pi m^{A,B} k_B T}. \tag{A4}$$

The potential energy terms ϕ can be divided into two contributions. The first is a repulsive part, which results from the hard cores of the particles. This we take to be infinite inside the cores and zero outside. We assume both A and B have the same diameter b, giving a total excluded volume of bN. The second is an attractive part, which we assume to be spatially constant. When the spatial integrations are performed in Eq. (A3), the exponential term goes to zero inside the excluded volume of either A or B, and to a constant, a_{AA}, a_{AB}, a_{BA}, or a_{BB}, outside. Therefore,

$$Z = \frac{(L-bN)^N}{N_A!\,N_B!}\left[\sqrt{2\pi m^A k_B T}e^{-(1/k_BT)(a_{AA}+a_{AB})}\right]^{N_A} \times \left[\sqrt{2\pi m^B k_B T}e^{-(1/k_BT)(a_{BA}+a_{BB})}\right]^{N_B}. \quad \text{(A5)}$$

Using Stirling's formula $[\ln(N!) \simeq N\ln(N) - N]$ in the above expression, we derive the following free energy:

$$\begin{aligned}\mathcal{F} &= -k_BT\ln(Z)\\ &= k_BT[N_A\ln(N_A) + N_B\ln(N_B)\\ &\quad - N\ln(L-bN)] + a_{AA}N_A + a_{AB}N_A + a_{BA}N_B + a_{BB}N_B.\end{aligned} \quad \text{(A6)}$$

We neglect terms that are constant or proportional to N^A or N^B, since they do not affect the physics within the system; they simply add an arbitrary constant to the pressure or chemical potential.

To capture the salient features of our system, we introduce an attractive van der Waals potential a, which gives rise to the liquid/gas phase transition, and a repulsive potential λ, which acts between unlike particles. To a first approximation, the strength of the interaction is proportional to the density, so we propose the mean field potentials to be of the form

$$a_{AA} = -a\frac{N_A}{L}, \quad a_{AB} = (2\lambda - a)\frac{N_B}{L},$$

$$a_{BA} = (2\lambda - a)\frac{N_A}{L}, \quad a_{BB} = -a\frac{N_B}{L}. \quad \text{(A7)}$$

Substituting these into Eq. (A6) and dividing by L gives the free energy density (2). In this study, we define the A and B particles to have equal mass and we choose the mass scale such that $m = m_A = m_B = 1$.

[1] D. Vollmer, J. Vollmer, and A. J. Wagner, Phys. Chem. Chem. Phys. **4**, 1380 (2002), and references therein.

[2] A. J. Bray, Adv. Phys., **43**, 357 (1994).

[3] R. Mendoza, I. Savin, K. Thornton, and P. W. Voorhees, Nat. Mater., **3**, 385 (2004).

[4] Felix Petlyuk and F. B. Petlyuk, *Distillation Theory and Its Application to Design of Separation Units* (Cambridge University Press, Cambridge, U.K., 2004).

[5] V. Talanquer and D. W. Oxtoby, J. Chem. Phys. **104**, 1993 (1996).

[6] P. R. ten Wolde and D. Frenkel, J. Chem. Phys. **109**, 9919 (1998).

[7] I. Napari and A. Laaksonen, J. Chem. Phys. **111**, 5485 (1999).

[8] A. Onuki, Phys. Rev. E **55**, 403 (1997).

[9] L. D. Landau and E. M. Lifshitz, *Fluid Mechanics*, 2nd ed., (Pergamon Press, New York, 1987).

[10] D. J. Holdych, D. Rovas, J. G. Georgiadis, and R. O. Buckius, Int. J. Mod. Phys. C **9**, 1393 (1998).

[11] M. R. Swift, E. Orlandini, W. R. Osborn, and J. M. Yeomans, Phys. Rev. E **54**, 5041 (1996).

[12] K. Huang, *Statistical Mechanics*, 1st ed. (Wiley, New York, 1963).

[13] For very large values of τ_ρ it was discovered that anisotropy was a problem. The tentacles were found to grow in preferred lattice directions. Therefore, care was taken in the high viscosity simulations to reduce the time step Δt, such that $\tau_\rho < 2$.

[14] A. Karim, J. F. Douglas, G. Nisato, D. W. Liu, and E. J. Amis, Macromolecules **32**, 5917 (1999).

[15] To produce this plot, the chemical potential contribution was removed from the free energy density such that the coexisting states have the same energy. In reality, the energy of the liquid is much higher, however, this does not change the arguments presented.

[16] M. Stamm and D. W. Schubert, Annu. Rev. Mater. Sci. **25**, 325 (1995).

[17] W. R. Osborn, E. Orlandini, M. R. Swift, J. M. Yeomans, and J. R. Banavar, Phys. Rev. Lett. **75**, 4031 (1995).